

Collimated Fast Wind in the Pre-Planetary Nebula CRL 618

Chin-Fei Lee¹, Ming-Chien Hsu¹, and Raghvendra Sahai²

ABSTRACT

Collimated fast winds (CFWs) have been proposed to operate during the post-AGB evolutionary phase (and even earlier during the late AGB phase), responsible for the shaping of pre-planetary nebulae (PPNs) and young planetary nebulae (PNs). This paper is a follow-up to our previous study of CFW models for the well-studied PPN CRL 618. Previously, we compared our CFW models with optical observations of CRL 618 in atomic and ionic lines and found that a CFW with a small opening angle can readily reproduce the highly collimated shape of the northwestern (W1) lobe of CRL 618 and the bow-like structure seen at its tip. In this paper, we compare our CFW models with recent observations of CRL 618 in CO J=2-1, J=6-5, and H₂ 1-0 S(1). In our models, limb-brightened shell structures are seen in CO and H₂ at low velocity arising from the shocked AGB wind in the shell, and can be identified as the low-velocity (LV) components in the observations. However, the shell structure in CO J=2-1 is significantly less extended than that seen in the observations. None of our models can properly reproduce the observed high-velocity (HV) molecular emission near the source along the body of the lobe. In order to reproduce the HV molecular emission in CRL 618, the CFW is required to have a different structure. One possible CFW structure is the cylindrical jet, with the fast wind material confined to a small cross section and collimated to the same direction along the outflow axis.

Subject headings: planetary nebulae: general – stars: AGB and post-AGB — stars: mass loss – stars: winds and outflows

1. Introduction

At the end of the evolution of low- and intermediate-mass stars, pre-planetary nebulae (PPNs) are seen associated with post asymptotic giant branch (post-AGB) stars. They will turn into planetary nebulae (PNs) in less than 1000 years as the post-AGB stars become hot white dwarfs. Their shaping mechanism is still unclear and is closely related to the mass-loss processes during the end phases of the evolution.

¹Academia Sinica Institute of Astronomy and Astrophysics, P.O. Box 23-141, Taipei 106, Taiwan; cflee@asiaa.sinica.edu.tw

² Jet Propulsion Laboratory, MS 183-900, 4800 Oak Grove Drive, Pasadena, CA 91109

Many PPNs and young PNs were found to have highly aspherical shapes, with a significant fraction having highly collimated bipolar or multipolar lobes (Corradi & Schwarz 1995; Schwarz et. al. 1997; Sahai & Trauger 1998; Sahai 2001; Sahai et al. 2007). Point symmetry, rather than axisymmetry, better characterizes the geometry of the majority of these objects [striking examples are He 2-115 (Sahai & Trauger 1998) and He 3-1475 (Borkowski, Blondin, & Harrington 1997)]. As a result, instead of spherical fast winds as in the generalized interacting stellar winds (GISW) model (see e.g., review by Balick & Frank 2002), collimated fast winds have been proposed to operate during the post-AGB phase (and even earlier during the late AGB phase), and be the primary agents for the shaping of PPNs and young PNs (Sahai & Trauger 1998; Sahai 2001). Collimated fast wind (CFW) models have been used to account for the morphology and kinematics of a few well-studied PPNs and PNs, with some assuming a radial wind with a small opening angle (Lee & Sahai 2003, hereafter Paper I; Akashi & Soker 2008), some assuming a cylindrical jet either unmagnetized (Cliffe et al. 1995; Steffen & López 1998; Guerrero et al. 2008) or magnetized (Lee & Sahai 2004), and some assuming a bullet (a massive clump) along the outflow axis (Dennis et al. 2008).

This paper is a follow-up to our previous study of CFW models for the well-studied PPN CRL 618 (Paper I). CRL 618 is located at a distance of 900 pc (Goodrich 1991). It shows several narrow lobes at different orientations in HST images (Trammell & Goodrich 2002) and belongs to the “multipolar” morphological classification (Sahai et al. 2007), perhaps resulting from multiple ejections at different orientations. The general structures of the different lobes are similar and we focus only on the northwestern (W1) lobe, which seems to be better separated from other lobes. In Paper I, we compared our CFW models with optical observations of CRL 618 in atomic and ionic lines and found that a CFW with a small opening angle can readily reproduce the highly collimated shape of the W1 lobe and the bow-like structure seen at its tip (Sánchez Contreras, Sahai, & Gil De Paz 2002). However, it may have difficulties in reproducing properly the high-velocity optical emission along the body of the lobe. In this paper, we compare our CFW models with recent observations of CRL 618 in H₂ 1-0 S(1) (Cox et al. 2003), CO J=2-1 (Sánchez Contreras et al. 2004) and J=6-5 (Nakashima et al. 2007). We find that our CFW models also have difficulties in reproducing the high-velocity molecular emission in the W1 lobe and the CFW is required to have a different physical structure.

2. Numerical Methods and Physical Settings

The two-dimensional hydrodynamic code, ZEUS 2D, is used for the simulations of our models, as in Paper I. This code has been now modified to include molecular cooling and the time dependent chemistry of hydrogen by solving the following equations (see also Suttner et al. 1997):

$$\frac{\partial e}{\partial t} + \nabla(e \cdot \mathbf{v}) = -p\nabla \cdot \mathbf{v} - \Lambda_A(T, n, f, g) - \Lambda_M(T, n, f, g) \quad (1)$$

$$\frac{\partial(fn)}{\partial t} + \nabla(fn \cdot \mathbf{v}) = R(T, n, f, g) - D(T, n, f, g) \quad (2)$$

$$\frac{\partial(gn)}{\partial t} + \nabla(gn \cdot \mathbf{v}) = I(T, n, f, g) - C(T, n, f, g) \quad (3)$$

where e , p , \mathbf{v} , and T are the internal energy density, thermal pressure, velocity, and temperature, respectively. Also, n is the hydrogen nuclei density, f is the fractional part of hydrogen molecules with $n_{\text{H}_2} = fn$ (i.e., $f = 0$ for atomic/ionic gas and $f = 0.5$ for molecular gas), and g is the fractional part of ionized hydrogen with $n_{\text{H}^+} = gn$. Helium is included as a neutral component with $n_{\text{He}} = 0.1n$ and thus $n = \rho/(1.4m_{\text{H}})$, where ρ and m_{H} are the mass density and the mass of atomic hydrogen, respectively. Here D and R are dissociation and reassociation rates of molecular hydrogen, respectively (see Suttner et al. 1997, and reference therein), I and C are ionization and recombination rates of atomic hydrogen, respectively. Λ_A is the optically thin radiative cooling from atoms and ions (as in Paper I), with the cooling at high temperature from MacDonald & Bailey (1981) and low temperature from Dalgarno & McCray (1972). Λ_M is the optically thin radiative cooling from molecules, including H_2 (Hollenbach & McKee 1979) and CO (McKee et al. 1982; Hollenbach & McKee 1989). The chemistry of CO is not included. The CO abundance is assumed to be constant and equal to 2×10^{-4} of the number of hydrogen molecules, as in Sánchez Contreras et al. (2004). We believe this assumption does not significantly affect our conclusions, it only affects the small-scale structure of the CO emission. The equations of state and material coefficients are (for similar derivation see Suttner et al. 1997):

$$\begin{aligned} p &= \frac{\rho k T}{\mu m_{\text{H}}} & e &= \frac{\rho C_v k T}{m_{\text{H}}} \\ \mu &= \frac{1.4}{1.1 - f + g} & C_v &= \frac{3.3 - f + 3g}{2.8} \end{aligned} \quad (4)$$

where k , μ , and C_v are the Boltzmann constant, mean molecular weight, and specific heat, respectively. A scalar color tracer c is also included in the simulations to track the fast wind, it is one for the fast wind, zero for the AGB wind, and a value between one and zero for a mixture of the fast wind and AGB wind. As in Paper I, the simulations are performed in spherical coordinates but presented in cylindrical coordinates (z , R), with the z -axis being the outflow axis.

Our CFW models are based on models 1 and 4 in Paper I, which were found to be the best models for the W1 lobe of CRL 618 as seen at optical wavelengths. In these models, a CFW with a small opening angle is assumed to emanate radially from the vicinity of the post-AGB star, interacting with a spherical AGB wind (for details see Paper I). In our simulations, the CFW is launched from the inner boundary of the simulation domain, which is at 5×10^{15} cm (~ 333 AU) away from the post-AGB star. The AGB wind is assumed to be molecular with a temperature of 10 K and have a mass-loss rate of $3 \times 10^{-5} M_{\odot} \text{ yr}^{-1}$ with an expansion velocity of 20 km s^{-1} . The CFW is assumed to have a mass-loss rate of $2.5 \times 10^{-7} M_{\odot} \text{ yr}^{-1}$, a speed of 300 km s^{-1} , and an opening angle of 10° . It can either be steady or pulsed with a temporal variation in the density and velocity (see Table 1). It can be either atomic or molecular, depending on the temperature of the CFW to be assumed.

3. Recent Observations in CO and H₂

CRL 618 has been recently observed in H₂ 1-0 S(1) at $\sim 0''.5$ resolution (Cox et al. 2003) and in CO J=2-1 (Sánchez Contreras et al. 2004) and J=6-5 (Nakashima et al. 2007) at $\sim 1''$ resolution (see Figs. 1 and 2). It is multipolar, but here we focus only on its W1 lobe that extends $\sim 6''$ to the west from the source. The systemic velocity in this region is -21.5 km s^{-1} LSR and the W1 lobe is mainly redshifted with a velocity ranging from -40 to 150 km s^{-1} LSR. The CO and H₂ emission toward the W1 lobe can be roughly separated into two components: a slow or low-velocity (LV) component with a velocity lower than $\sim 20\text{--}30 \text{ km s}^{-1}$ from the systemic and a fast or high-velocity (HV) component with a velocity extending to $\sim 170 \text{ km s}^{-1}$ from the systemic. The LV component is extended. In CO J=2-1, it forms a limb-brightened shell structure around the optical lobe, extending to $\sim 5''$ away from the source. In CO J=6-5, it also forms a shell structure but only in the southern part of the lobe, extending to only $\sim 3''$ away from the source. As discussed in Nakashima et al. (2007), however, it should be more extended, because most of the extended flux has been resolved out in their observations. In H₂, it is spatially unresolved, extending mainly from $2''$ to $6''$ from the source, slightly ahead of that seen in CO J=2-1. On the other hand, the HV component is more compact. In CO J=2-1, it extends to $\sim 2''.5$ away from the source with the velocity increasing linearly with the distance from near the systemic velocity to the highest velocity. In H₂, it is seen with three localized emission peaks separated by $\sim 2''$: (1) a peak close to the source with a range of (blueshifted and redshifted) velocities, (2) a bright peak at $\sim 2''.5$, where the tip of the CO HV component is, with a broad range of velocities extending from near the systemic velocity to the highest velocity, and (3) a faint peak at $\sim 4''$ at $\sim 80 \text{ km s}^{-1}$ LSR.

4. Results

In the following, we present our models and the comparison with the observations. Figure 3 shows the distributions of hydrogen nuclei density and temperature with molecular fraction in our models at the age of ~ 160 yrs, when the outflow lobe has a length of ~ 6000 AU, similar to the deprojected length of the W1 lobe of CRL 618. The separation between the AGB wind and the CFW is delineated by the color tracer $c = 0.5$, at which half is the AGB wind and half is the CFW. In order to compare with the observations, we also derive intensity maps of the LV and HV components (Fig. 4) and position velocity (PV) diagrams (Fig. 5) for the CO J=2-1, J=6-5, and H₂ 1-0 S(1) emission from our models, assuming the latter to be optically thin and arising from gas in local thermal equilibrium (LTE). We assume a distance of 900 pc and an inclination of 30° , values appropriate for CRL 618 (Sánchez Contreras et al. 2004). The HV components are derived by integrating the emission with velocity higher than 50 km s^{-1} from the systemic and the LV components by integrating the emission with velocity within 50 km s^{-1} from the systemic. Two angular resolutions, $0''.1$ and $0''.5$, are assumed, with the latter for comparing with the current observations.

4.1. Model 1: Steady Atomic CFW at 10,000 K

Model 1 here corresponds to model 1 in Paper I. The CFW has a temperature of 10^4 K and is thus atomic. As it blows into the AGB wind, it produces a collimated outflow lobe, which is a thin shell with a cavity (Fig. 3a). As shown, the shell consists of shocked AGB wind in the outer shell and shocked fast wind in the inner shell (Fig. 3A). Since the shell is already radiative and thus momentum-driven even without molecular cooling, additional molecular cooling does not change the shell dynamics, it only reduces the shell thickness as compared to that in Paper I. In the shell, the shock becomes stronger going from near the source toward the tip of the lobe. As a result, the temperature of the shock AGB wind increases from tens K near the source to above 10^4 K near the tip (Fig. 3b). In addition, the shocked AGB wind is mainly molecular near the source but becomes mainly atomic near the tip (except for the newly shocked AGB wind) because of shock dissociation. In contrast, the shocked fast wind is mainly atomic.

In the simulation, a jet-like structure is seen at the tip because of the accumulation of material there due to the shock focusing effect, as discussed in Paper I. Such accumulation might be artificially enhanced in our 2D simulations because material cannot flow across the symmetry axis. This enhancement in turn would lead to more cooling and further accumulation, and then an increase in the formation rate of molecules. Therefore, the molecular emission from the lobe tip might be highly overestimated and should be kept in mind when comparing our models to the observations.

In this model, the LV components of the CO J=2-1, J=6-5, and H₂ emission are seen forming limb-brightened shell structures around the cavity (Fig. 4, model 1), as in the CO observations (Fig. 1). They arise from the shocked AGB wind in the shell. Since the temperature in the shell increases with the distance from the source, the shell structure extends further and further away from CO J=2-1 to CO J=6-5 and to H₂. The CO J=2-1 emission traces the cold (20-100 K) gas extending to $\sim 2''$ from the source, the CO J=6-5 emission traces the warm gas (50-300 K) extending to $\sim 3''$, and the H₂ emission traces the hot gas (~ 2000 K) extending from $3''$ to $5''$. In CO J=2-1, however, the shell structure in this model is significantly less extended than that seen in the observations (Fig. 1), indicating that the temperature in the shell in this model must have decreased less rapidly from the tip to the source than that in the observations. No HV component is seen in this model due to the lack of molecules at high velocity, except for the jet-like structure at the tip of the lobe.

PV diagrams of CO and H₂ emission cut along the outflow axis together show a V-shaped PV structure extending to ~ 40 km s⁻¹ from the systemic, with the CO emission at the lower end and the H₂ emission at the upper end (Fig. 5, model 1). This PV structure is associated with the LV components, arising from the shocked AGB wind in the shell, which is in the expanding lobe. This PV structure is expected, with the left and right parts from the back and front walls of the expanding lobe, respectively. In observations, the LV component in CO J=2-1 also shows a hint of a V-shaped PV structure (Fig. 2) and has also been modeled with an expanding lobe by Sánchez Contreras et al. (2004). The expansion velocity in their model, however, is ~ 22 km s⁻¹,

much lower than that in our model. The upper end of the V-shaped PV structure is also expected to be seen in H_2 even at low resolutions in the observations (Fig. 5, model 1). However, no such PV structure is seen in H_2 observations (Fig. 2). It is likely because the outflow lobe in CRL 618 indeed has a smaller expansion velocity as found in the CO J=2-1 observations, so that the V-shaped PV structure could have been smeared out in the observations.

4.2. Model 2: Pulsed Atomic CFW at 10,000 K

Model 2 here corresponds to model 4 in Paper I. The CFW here is the same as that in model 1 but with a temporal variation in density and velocity with an amplitude $A = 0.5$ (i.e., $\Delta v = 150 \text{ km s}^{-1}$) and a period $P = 22 \text{ yr}$ (see Paper I). In this model, a series of internal shock pairs are formed in the cavity moving along the outflow axis at high velocity, as the faster CFW catches up with the slower CFW (Figs. 3c, d). They are mainly atomic. They do not affect the shell dynamics. They only produce small disturbances (ripples) on the shell structure in the regions where the internal shocks interact with the shell. Thus, the emission structures in CO and H_2 are the same as in model 1, except that there are faint ring-like structures seen across the cavity arising from the ripples in the shell (Fig. 4). The PV diagrams are also similar to those in model 1, except that there are faint low-velocity H_2 emission near the source arising from the ripples in the shell (Fig. 5). No HV component is seen from the internal shocks due to the lack of molecules. As a result, although this model was found to produce optical emission in the cavity with the internal shocks (Paper I), it can not produce molecular emission in the cavity.

4.3. Model 3: Steady Molecular CFW at 1000 K

This model is the same as model 1 but with the CFW assumed to be molecular at 1000 K, in order to have HV molecular gas inside the cavity. Note that the assumed value of the temperature is not important, because the temperature of the CFW will drop rapidly below 100 K in 200 AU (or $\sim 0''.2$) due to radial expansion and radiative cooling (Fig. 3f). Since the shell is not pressure-driven, reducing the temperature of the CFW does not change the shell dynamics (Fig. 3e). Thus, the molecular fraction of the shocked AGB wind in the shell is the same as in model 1, and so are the emission and PV structures of the LV components (Figs. 4 and 5). On the other hand, only the newly shocked fast wind in the inner boundary of the shell is molecular (as indicated by the contours of f , Fig. 3C) since the shock there is weak. It is hot, producing two HV shell structures in H_2 at the far end, one at $\sim 3''.5$ around $\sim 60 \text{ km s}^{-1}$ and one at $\sim 5''$ around $\sim 100 \text{ km s}^{-1}$, with the velocity increasing with the distance from the source. The one at $\sim 3''.5$ may have a counterpart at $\sim 4''$ in the H_2 observations (see Figs. 1 and 2). Since the temperature of the CFW itself drops below 100 K in 200 AU, HV CO emission is seen arising from the CFW itself near the source. However, due to radial expansion of the CFW itself, this HV CO emission is very faint as compared with the LV component in the PV diagrams at the resolutions of the observations (Fig.

5), inconsistent with the observations, in which the HV CO component is comparable to the LV component (Fig. 2). Besides, no HV H₂ emission is seen from the CFW itself near the source.

4.4. Model 4: Pulsed molecular CFW at 1000 K

This model is the same as model 3 but with the CFW assumed to have a temporal variation in density and velocity with an amplitude $A = 0.5$ (i.e., $\Delta v = 150 \text{ km s}^{-1}$) and a period $P = 22 \text{ yr}$. As in model 2, the shell structure and dynamics are not affected much by the internal shocks (Figs. 3g, h). Thus, the emission and PV structures of the LV components, which arises from the shocked AGB wind in the shell, are also similar to those in model 2. The internal shocks, as they propagate beyond 1000 AU ($\sim 1''$) from the source, become strong enough to dissociate the molecules (Fig. 3D). Therefore, only the internal shock closer to $\sim 1''$ produces HV H₂ emission (Figs. 4 & 5). These internal shocks are so strong that the molecules in the newly shocked fast wind in the inner boundary of the shell at the end of the lobe are also dissociated. Thus, unlike model 3, no HV H₂ emission is seen from the newly shocked fast wind at the far end.

4.5. Model 5: Pulsed Molecular CFW at 1000 K with $A = 0.3$

This model is the same as model 4, but with a smaller variation amplitude with $A=0.3$ (i.e., $\Delta v = 90 \text{ km s}^{-1}$). In this case, the internal shocks are weaker, so that molecules can survive in the internal shocks except at their tips (Figs. 3i, j, E, see the contours of f). Therefore, HV H₂ emission is seen arising from the internal shocks, with the intensity decreasing rapidly with the distance due to radial expansion (Fig. 4). It is seen arising from the first three internal shocks, forming three HV emission clumps (or knots) that may correspond to the three HV H₂ emission peaks seen in the H₂ observations (Fig. 1). The HV H₂ emission seen at $\sim 2''$ away from the source can be compared to that seen at similar distance in the observations. However, its kinematics, with the velocity increasing toward the tip and an emission peak at the highest velocity (Fig. 5), is inconsistent with the observations (Fig. 2). HV CO J=6-5 emission is seen from the wings of the internal shocks and may show similar PV structure to that seen in the observations. However, it is too weak (relative to the LV CO J=6-5 emission) to explain the observations. In addition, the internal shocks are too hot to have CO J=2-1 emission.

4.6. Model 6: Pulsed Molecular CFW at 1000 K with $A = 0.1$

This model is the same as model 5, but with a smaller variation amplitude with $A=0.1$ (i.e., $\Delta v = 30 \text{ km s}^{-1}$). In this case, the internal shocks become too weak to dissociate any molecules in the internal shocks (Figs. 3k, l). Molecules also can survive in the newly shocked fast wind in the inner boundary of the shell at the far end of the lobe, producing HV H₂ emission at the far end as

in model 3. The internal shocks are cold enough to have HV CO emission in J=6-5, but too cold to have HV H₂ emission and too hot to have HV CO emission in J=2-1. In addition, due to radial expansion, the intensity of the HV CO emission in J=6-5 at $\sim 2''$ is still too faint to be compared with the LV component (Fig. 5), inconsistent with the observations (Figs. 1 and 2). Moreover, there will be no atomic and ionic emission from the internal shocks, inconsistent with the optical observations that show atomic and ionic emission along the body of the lobe.

4.7. Summary of our models

In summary, limb-brightened shell structures are seen in our models in CO and H₂ at low velocity arising from the shocked AGB wind in the shell, and can be identified as the LV components in the observations. However, the shell structure in CO J=2-1 is significantly less extended than that seen in the observations. None of our models can properly reproduce the observed HV molecular emission near the source along the body of the lobe. In our models in which the CFWs are atomic, the shell has high-velocity molecular material only at the far end of the lobe. Thus, in order to produce HV molecular emission near the source, the CFW itself has to be molecular. In our steady CFW models, although there is some HV CO emission near the source from the CFW itself, it is far too weak (relative to the LV CO emission) to explain the observations. This is because the column densities of the HV molecular material decrease very rapidly due to radial expansion. In our pulsed CFW models, HV H₂ emission can be seen along the outflow axis arising from the internal shocks and may correspond to that seen in the observations. However, its kinematics is inconsistent with the observations. HV CO 6-5 emission can be seen arising from the internal shocks and may show similar PV structure to that seen in the observations. However, it is too weak (relative to the LV CO J=6-5 emission) to explain the observations. In addition, HV CO J=2-1 emission from the internal shocks is far too weak.

5. Discussion

5.1. Could the HV component be from a different lobe?

In high-resolution optical images, CRL 618 is clearly seen with multiple lobes on each side and some of these lobes are not as extended as the W1 lobe (see Fig. 1 and Trammell & Goodrich 2002). It is thus possible that the HV component is actually associated with a small lobe that happens to be aligned with the W1 lobe, and arises from the shell instead of the internal shocks. This small lobe could be either a highly inclined extended lobe that appears small in projection or a younger lobe that has a smaller physical linear extent compared to the W1 lobe. Our model 3, which has molecular emission from both the shocked AGB wind and shocked fast wind in the shell, can be used to investigate this possibility.

At a higher inclination of 60° , the outflow lobe has a projected length of $\sim 3''$. At this higher inclination, the emission from the shocked AGB wind has a higher velocity, but still much lower than the observed HV component (Fig. 6). The two HV H_2 emission from the shocked fast wind at the far end are now projected to $\sim 2''.5$ at $\sim 100 \text{ km s}^{-1}$ and $\sim 3''$ at $\sim 180 \text{ km s}^{-1}$, respectively. The one at $2''.5$ can be compared with the observed H_2 component at the same distance. However, its velocity increases with the distance, inconsistent with the observations. In addition, no HV CO emission is seen from the shocked fast wind. Only faint HV CO emission is seen near the source from the CFW itself.

At a younger age of 86 years, the outflow lobe also has a projected length of $\sim 3''$ at the inclination of 30° . The emission from the shocked AGB wind and shocked fast wind has the same velocity structure as at older age (Fig. 6), because the shell is momentum-driven and thus roughly self similar. The HV H_2 emission from the shocked fast wind at $\sim 2''$ may show a similar PV structure to that seen at $\sim 2''.5$ in the observations. However, no HV CO emission is seen from the shocked fast wind. Again, only faint HV CO emission is seen near the source from the CFW itself.

As a result, adding a small lobe into our models is still not able to reproduce the observed HV CO and H_2 components in CRL 618 properly. The HV molecular gas in CRL 618 might have a layered structure, with different temperatures and thus different emissions in different layers.

5.2. Could the CFW have a different physical structure?

The CFW may have a different physical structure, as concluded in Paper I when comparing optical emission along the body of the lobe in our models to the observations. Here we discuss the two possible physical structures of the CFW that have been studied in the literature.

5.2.1. Episodic Cylindrical jet?

The CFW could be in a form of a cylindrical jet, with the fast wind material confined to a small cross section and collimated to the same direction along the outflow axis. In this case, the CFW has a constant density with the distance from the source. The observations in CO J=2-1 also show that the HV component is better reproduced by a cylinder with the gas flowing axially (Sánchez Contreras et al. 2004). Simulations with episodic cylindrical jets have been performed by a number of authors in order to reproduce the morphology and kinematics of protostellar outflows (e.g., Suttner et al. 1997; Lee et al. 2001). Such jets can also produce a series of internal bow shocks with HV CO and H_2 emissions along the body of the lobe (Suttner et al. 1997). Without radial expansion, the emission of these bow shocks does not decrease as fast as that in our current models. In addition, unlike those in our current models, the shocks are ballistic (Lee et al. 2001). The cylindrical jet models have been applied to PNs (Cliffe et al. 1995; Steffen & López 1998; Lee & Sahai 2004; Guerrero et al. 2008) and may apply to PPNs as well.

The jet is likely to be magnetized because the magnetic field can provide the required collimation. In addition, a magnetized jet has also been found to better reproduce the jet emission in the young PN Hen 2-90 than an unmagnetized jet (Lee & Sahai 2004). The jet could be launched by magneto-centrifugal forces from a magnetized accretion disk and star system (Blackman, Frank, & Welch 2001), like the protostellar jets (Shu et al. 1994; Konigl & Pudritz 2000). The central star could have a binary companion and the accretion disk could form as the material flows to the companion (Mastrodemos & Morris 1998).

5.2.2. *Bullet?*

Recently, a bullet (i.e., a massive clump) model has also been proposed for PPN shaping because it can also produce a collimated outflow lobe (Dennis et al. 2008). The bullet could be launched by an explosive MHD mechanism (see, e.g., Matt et al. 2006). It is not clear, however, how a bullet can produce HV molecular emission near the source along the body of the lobe. One way that we can think of is to have a chain of bullets along the body of the lobe. Note that, however, a jet model with a periodic variation in velocity has been found to be better than a model with a chain of bullets or dense clumps, in reproducing the knotty jet emission in the young PN Hen 2-90 (e.g., comparing models 1 and 2 in Lee & Sahai 2004).

Dennis et al. (2008), having compared their jet and bullet models, argued that the bow-shock heads of bullets take on a V-shaped configuration and are thus more consistent with the observations of CRL 618, whereas bow-shock heads of jets are more U-shaped. However, the assumed density and thus the mass-loss rate of the AGB wind in their models are about a factor of 1000 less than those assumed in our models, which are more appropriate for CRL 618 (Knapp & Morris 1985; Sánchez Contreras et al. 2004). With a high density of the AGB wind as observed, the jet model has been found to produce V-shaped heads (see, e.g., Suttner et al. 1997; Lee et al. 2001) similar to that seen in CRL 618, because of efficient cooling at high density. The jet model in Dennis et al. (2008) may instead apply to another PPN OH 231.8+4.2, which shows a wide and more U-shaped outflow lobe (Bujarrabal et al. 2002).

5.3. **Is the CFW molecular?**

In our models, the CFW is assumed to be molecular in order to have HV molecular emission near the source along the body of the lobe. It could be intrinsically molecular. It could also be intrinsically atomic and become molecular right after launched due to its high mass-loss rate, as proposed for protostellar wind (Glassgold et al. 1991). Alternatively, the HV molecular emission could arise from the entrained AGB material that was originally close to the source, as suggested by Cox et al. (2003), or in the inner dense torus-like core around the source, as suggested by Sánchez Contreras et al. (2004). It is not clear in our simulations, however, how this entrainment

can happen once the shell is formed and shields the fast wind from being interacting with the AGB wind around the source. It probably can happen if the fast wind is actually launched from around a binary companion. As the AGB wind flows to the companion, an accretion disk can form (Mastrodemos & Morris 1998) and launch the fast wind, and then the fast wind can entrain the AGB wind.

6. Conclusions

We have presented simulations of CFW models including molecular cooling and time dependent chemistry of hydrogen. We have also derived from our simulations intensity maps and position velocity diagrams for CO J=2-1, J=6-5, and H₂ 1-0 S(1) emission and compared them to recent observations of CRL 618. In our models, limb-brightened shell structures are seen in CO and H₂ at low velocity arising from the shocked AGB wind in the shell, and can be identified as the low-velocity (LV) components in the observations. However, the shell structure in CO J=2-1 is significantly less extended than that seen in the observations. None of our models can properly reproduce the observed high-velocity (HV) molecular emission near the source along the body of the lobe. In order to reproduce the HV molecular emission, the CFW is required to have a different structure. One possible CFW structure is the cylindrical jet, with the fast wind material confined to a small cross section and collimated to the same direction along the outflow axis.

C.-F. Lee and M.-C. Hsu are financially supported by the NSC grant NSC96-2112-M-001-014-MY3. RS thanks NASA for funding this work via an LTSA award (NMO710840-102898); RS also received partial support for this work from an HST GO award (no. GO-10317.01) from the Space Telescope Science Institute (operated by the Association of Universities for Research in Astronomy, Inc., under NASA contract NAS5-26555). Some of the research described in this paper was carried out by RS at the Jet Propulsion Laboratory, California Institute of Technology, under a contract with the National Aeronautics and Space Administration.

REFERENCES

- Akashi, M., & Soker, N. 2008, ArXiv e-prints, 805, arXiv:0805.2332
- Balick, B., & Frank, A. 2002, ARA&A, 40, 439
- Blackman, E. G., Frank, A., & Welch, C. 2001, ApJ, 546, 288
- Borkoski, K. J., Blondin, J. M., & Harrington, J. P. 1997, ApJ, 482, L97
- Bujarrabal, V., Alcolea, J., Sánchez Contreras, C., & Sahai, R. 2002, A&A, 389, 271
- Cliffe, J. A., Frank, A., Livio, M., & Jones, T. W. 1995, ApJ, 447, L49

- Corradi, R. L. M. & Schwarz, H. E. 1995, *A&A*, 293, 871
- Cox, P. et al., 2003, *AJ*, 586, L87
- Dalgarno, A. & McCray, R. A. 1972, *ARA&A*, 10, 375 *MNRAS*, 314, 241
- Dennis, T. J. et al., 2008, *AJ*, 679, 1327
- Glassgold, A. E., Mamon, G. A., & Huggins, P. J. 1991, *ApJ*, 373, 254
- Goodrich, R. W. 1991, *ApJ*, 376, 654
- Guerrero, M. A., et al. 2008, *ApJ*, 683, 272
- Hollenbach, D., & McKee, C. F. 1979, *ApJS*, 41, 555
- Hollenbach, D., & McKee, C. F. 1989, *ApJ*, 342, 306
- Knapp, G. R. & Morris, M. 1985, *ApJ*, 292, 640
- Konigl, A. & Pudritz, R. E. 2000, *Protostars and Planets IV*, 759
- Lee, C.F., Stone, J. M., Ostriker, E. C., & Mundy, L. G 2001, *ApJ*, 557, 429
- Lee, C.F., & Sahai, R., 2003, *ApJ*, 586, 319 (paper I)
- Lee, C.F., & Sahai, R., 2004, *ApJ*, 606, 483
- MacDonald, J. & Bailey, M. E. 1981, *MNRAS*, 197, 995
- Mastrodemos, N., & Morris, M. 1998, *ApJ*, 497, 303
- Matt, S., Frank, A., & Blackman, E. G. 2006, *ApJ*, 647, L45
- McKee, C. F., Storey, J. W. V., Watson, D. M., & Green, S. 1982, *ApJ*, 259, 647
- Nakashima, J. et al., 2007, *AJ*, 134, 2035
- Sahai, R. 2001, in *Post-AGB Objects as a Phase of Stellar Evolution*, ed. R. Szczerba & S.K. Gorny (Dordrecht:Kluwer),53
- Sahai, R.,& Trauger, J.T. 1998, *AJ*, 116, 1357
- Sahai, R., Morris, M., Sánchez Contreras, C., & Claussen, M. 2007, *AJ*, 134, 2200
- Sánchez Contreras, C., & Sahai, R. & Gil De Paz, A 2002, *ApJ*, 578, 269
- Sánchez Contreras, C., Bujarrabal, V., Castro-Carrizo, A., Alcolea, J., & Sargent, A.. 2004, *ApJ*, 617, 1142

- Schwarz, H. E., Aspin, C., Corradi, R. L. M., & Reipurth, B. 1997, *A&A*, 319, 267
- Shu, F., Najita, J., Ostriker, E., Wilkin, F., Ruden, S., & Lizano, S. 1994, *ApJ*, 429, 781
- Steffen, W., & Lopez, J. A. 1998, *ApJ*, 508, 696
- Suttner, G., Smith, M. D., Yorke, H. W., & Zinnecker, H. 1997, *A&A*, 318, 595
- Trammell, S. R., & Goodrich, R. W. 2002, *ApJ*, 579, 688

This preprint was prepared with the AAS L^AT_EX macros v5.2.

Table 1. Physical parameters of the CFWs

Model	Temperature (K)	Composition	Status
1	10^4	Atomic	Steady
2	10^4	Atomic	Pulsed with $A = 0.5$
3	10^3	Molecular	Steady
4	10^3	Molecular	Pulsed with $A = 0.5$
5	10^3	Molecular	Pulsed with $A = 0.3$
6	10^3	Molecular	Pulsed with $A = 0.1$

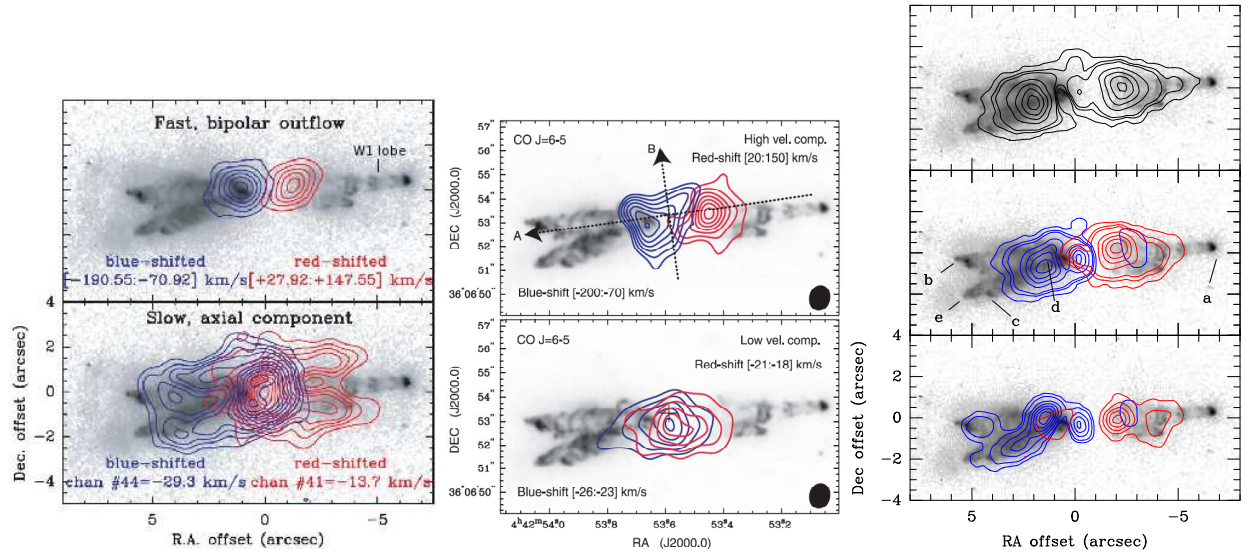


Fig. 1.— CO J=2-1, CO J=6-5, and H₂ 1-0 S(1) emission contours superposed on the HST optical image of CRL 618. (Left Column) The top and bottom panels show the contours of CO J=2-1 emission at high and low velocities, respectively (Sánchez Contreras et al. 2004). (Middle Column) The top and bottom panels show the contours of CO J=6-5 emission at high and low velocities, respectively (Nakashima et al. 2007). (Right Column) The top, middle, and bottom panels show the contours of H₂ 1-0 S(1) emission at low velocity, middle velocities, and high velocities, respectively (Cox et al. 2003). The source is either at the position offset (0,0) or marked by a cross. The W1 lobe is the optical lobe extending $\sim 6''$ to the west from the source, as indicated.

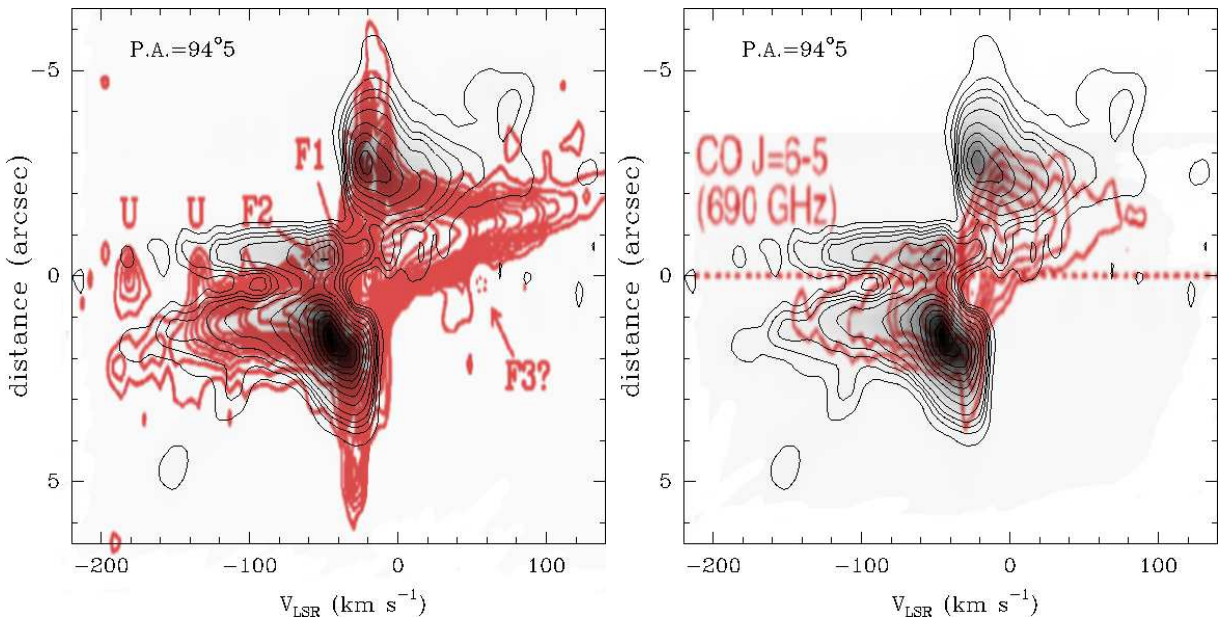


Fig. 2.— Position-velocity (PV) diagrams of H_2 (black contours with gray image in both panels, Cox et al. 2003), $\text{CO J}=2-1$ (red contours in the left panel, Sánchez Contreras et al. 2004), and $\text{CO J}=6-5$ (red contours in the right panel, Nakashima et al. 2007) emission cut along the outflow axis. The W1 lobe is mainly redshifted with a velocity ranging from -40 to 150 km s^{-1} LSR.

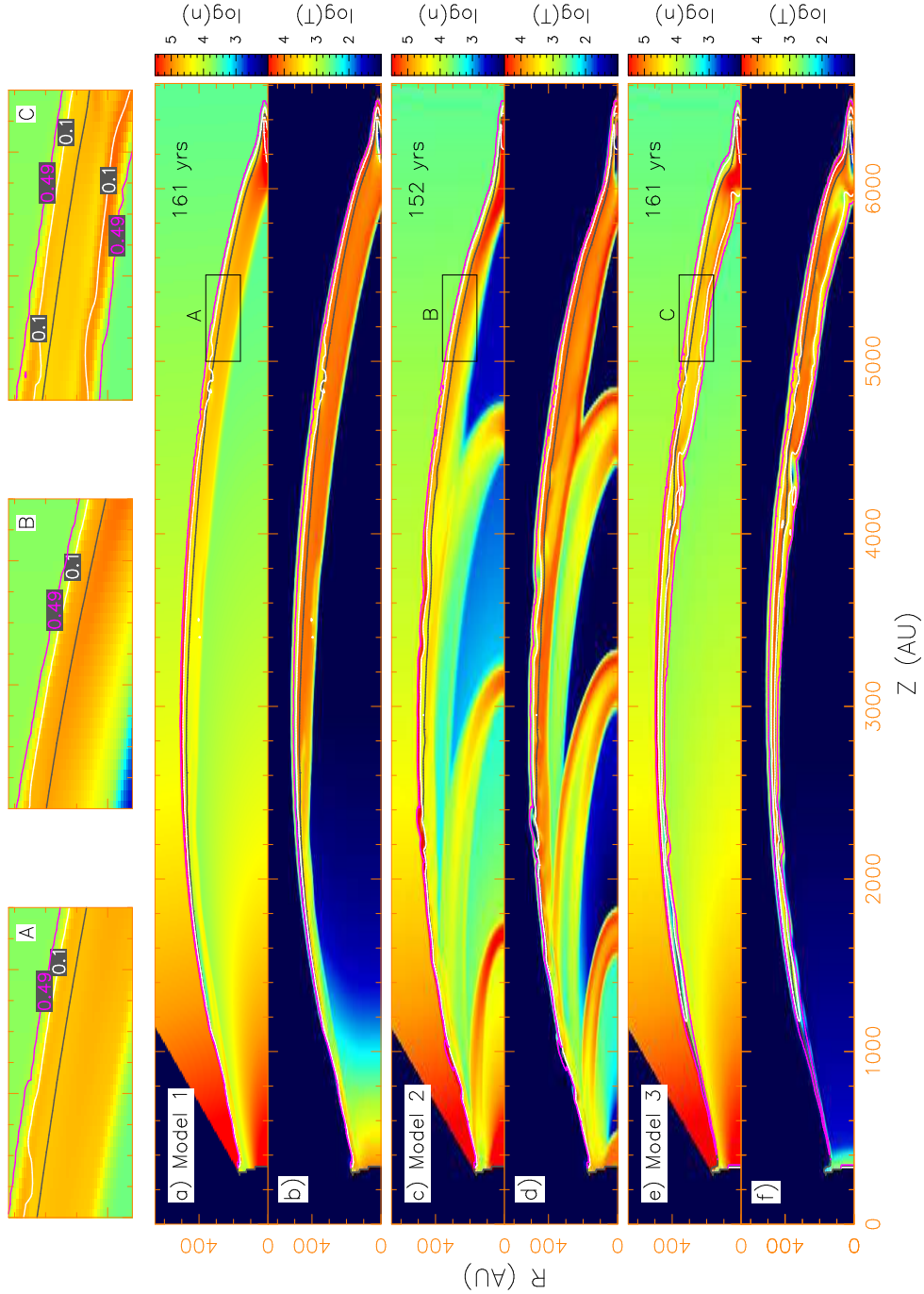


Fig. 3.— Simulations of our CFW models from 1 to 6, at the age of ~ 160 yrs. (a), (c), (e), (g), (i), and (k) show the number density of hydrogen nuclei in logarithmic scale. (b), (d), (f), (h), (j), and (l) show the temperature in logarithmic scale. The molecular fractions $f = 0.1$ (white line) and $f = 0.49$ (magenta line) are shown to outline the distribution of molecular gas. The separation between the AGB wind and the CFW is shown by the color tracer $c = 0.5$ (gray line, at which half is AGB wind and half is CFW). The CFW is atomic at 10,000 K in models 1 and 2, while is molecular at 1000 K in models 3, 4, 5, and 6. The CFW is steady in models 1 and 3, while is pulsed with $A=0.5$ in models 2 and 4, $A=0.3$ in model 5, and $A=0.1$ in model 6. (A)–(F) show respectively the blow-ups for the regions in the boxes A–F.

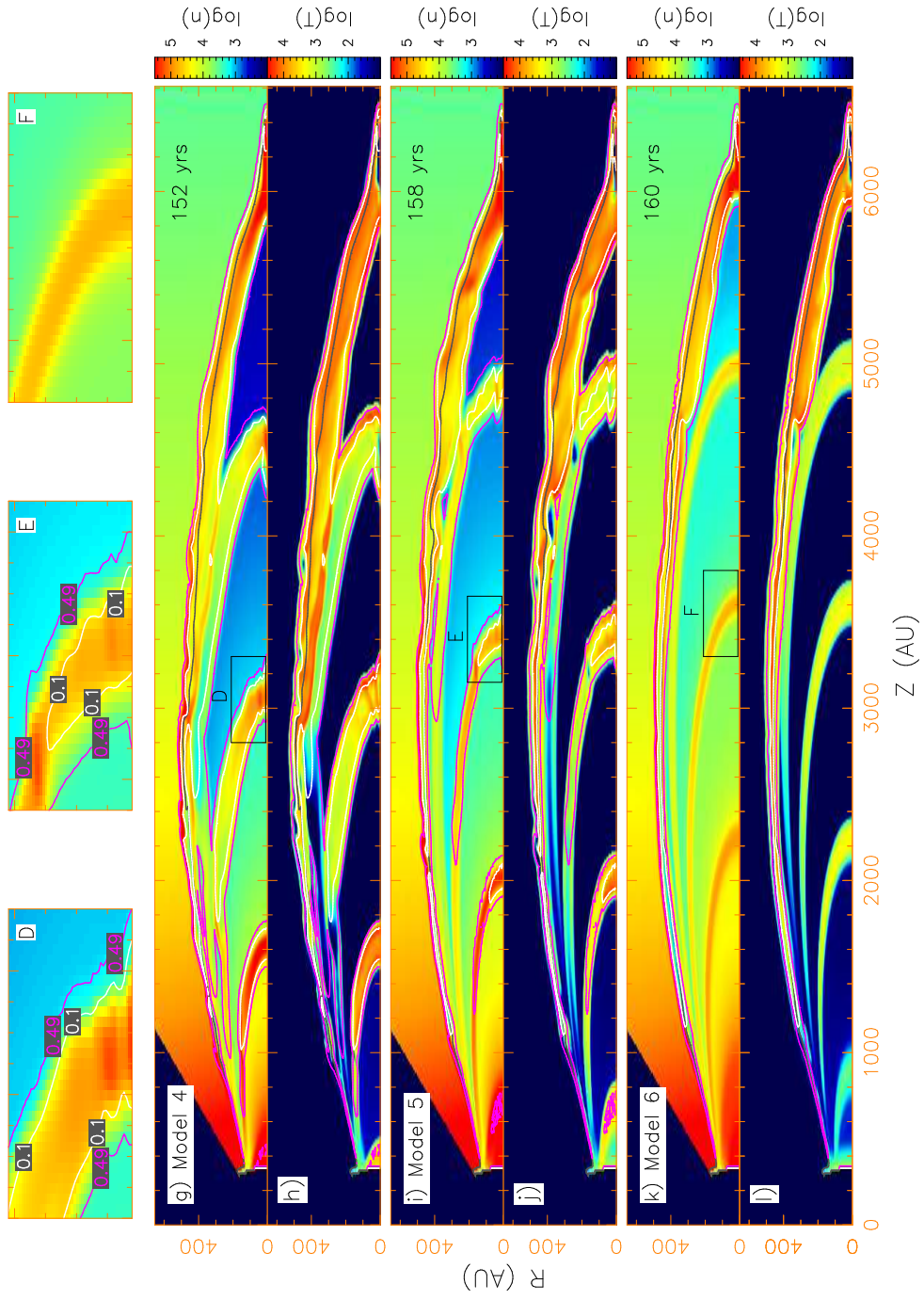


Fig. 3.— *Continued*

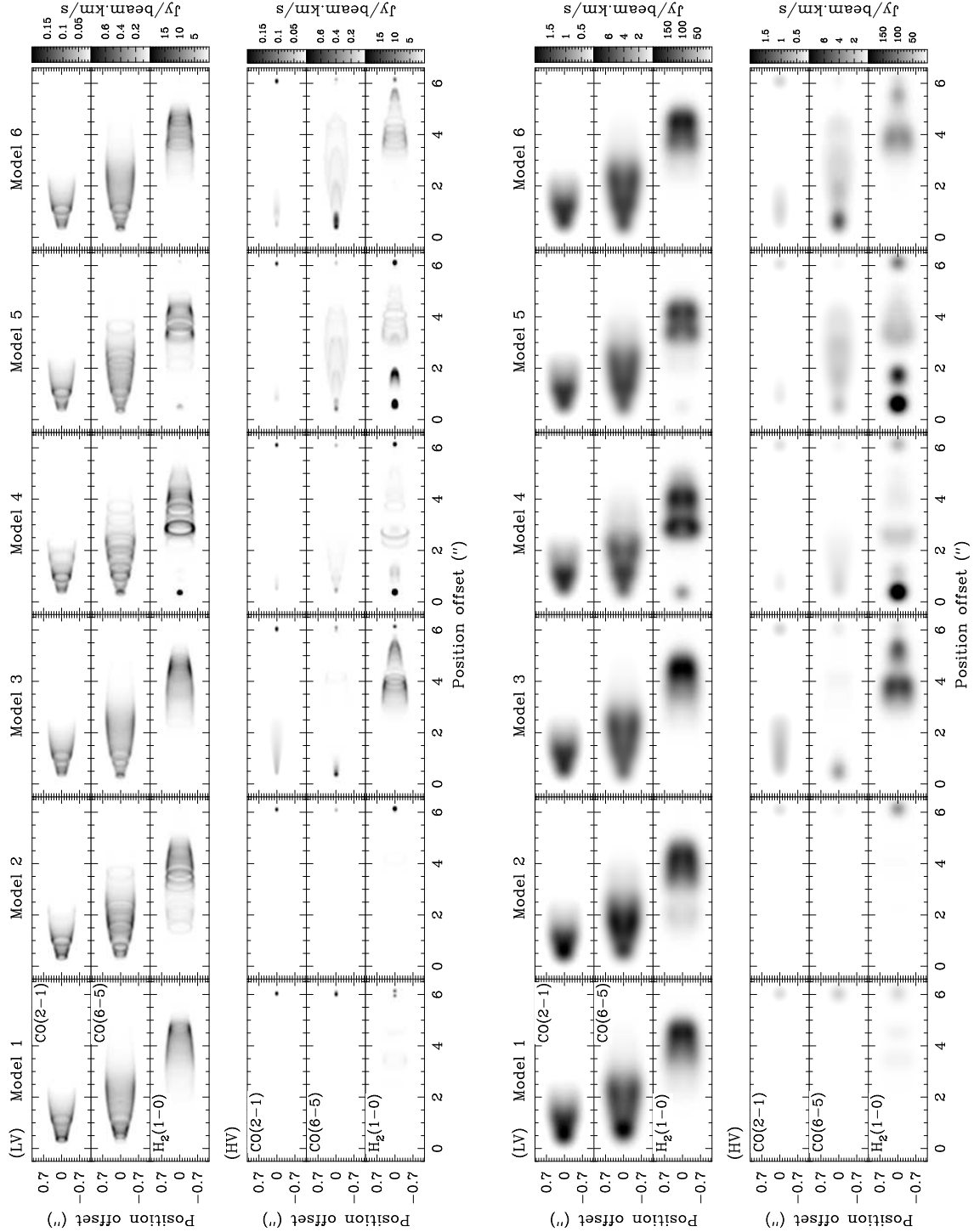


Fig. 4.— Integrated CO J=2-1 (top row), CO J=6-5 (middle row), and H₂ (bottom row) intensity maps derived from our models 1 to 6 from left column to right column. The first set and second set of panels show the LV and HV components at 0".1 resolution, respectively. The third set and fourth set of panels show the LV and HV components at 0".5 resolution, respectively, for comparing to the observations. The HV components are derived by integrating the emission with velocity higher than 50 km s⁻¹ from the systemic and the LV components by integrating the emission with velocity within 50 km s⁻¹ from the systemic.

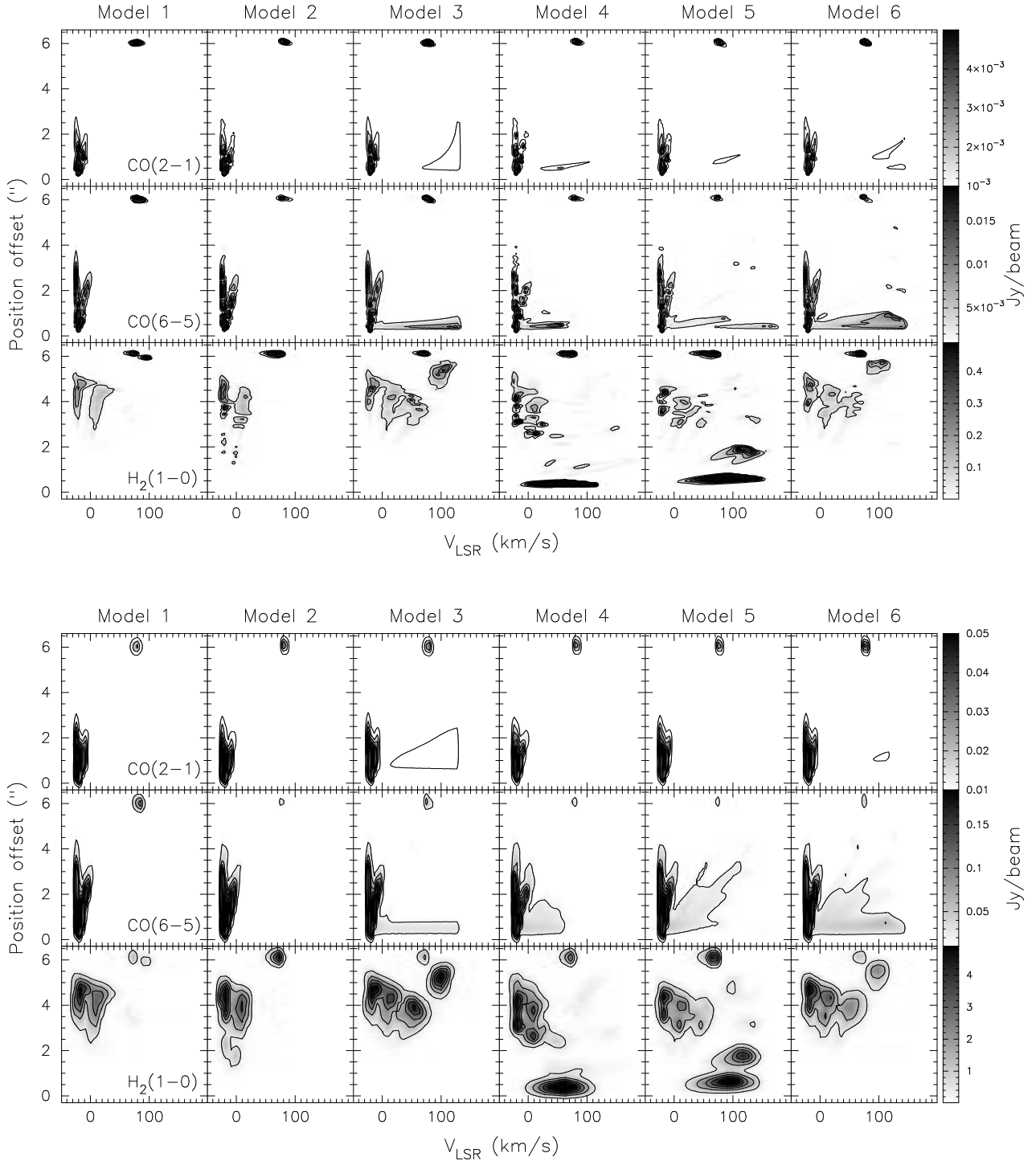


Fig. 5.— PV diagrams of CO $J=2-1$ (top row), CO $J=6-5$ (middle row), and H_2 (bottom row) emission cut along the outflow axis, derived from our models 1 to 6. Top set is derived with a spatial resolution of $0''.1$ and a velocity resolution of 4 km s^{-1} . Bottom set is derived with a spatial resolution of $0''.5$ and a velocity resolution of 5.2 km s^{-1} for CO and 9 km s^{-1} for H_2 emission, for comparing with the observations. The contours go from 10% to 90% with a step of 20% of the peak value.

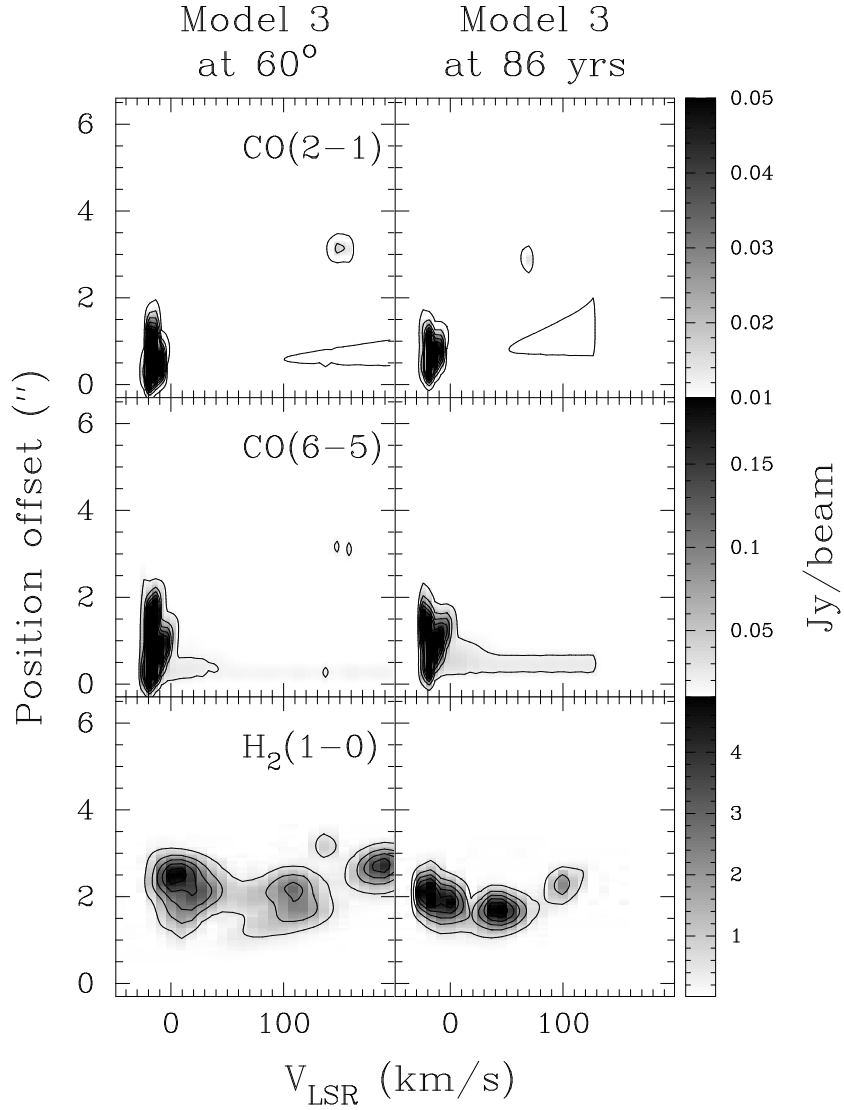


Fig. 6.— PV diagrams of CO $J=2-1$ (top row), CO $J=6-5$ (middle row), and H_2 (bottom row) emission cut along the outflow axis, derived from our model 3 at a higher inclination of 60° (left column) and a younger age of 86 yrs (right column). They are derived with a spatial resolution of $0''.5$ and a velocity resolution of 5.2 km s^{-1} for CO and 9 km s^{-1} for H_2 emission, for comparing with the observations. The contours go from 10% to 90% with a step of 20% of the peak value.